Progress In Electromagnetics Research B, Vol. 26, 69–100, 2010

CHANNEL MEASUREMENTS AND MODELLING IN A MILITARY CARGO AIRPLANE

C. G. Spiliotopoulos and A. G. Kanatas

Department of Digital Systems
University of Piraeus
80 Karaoli & Dimitriou St., Piraeus 18534, Greece

Abstract—The results of an ultrawideband (UWB) measurement campaign carried out in a Hercules C-130 military cargo airplane are presented. The environment encompasses several metallic surfaces resulting in a large number of multipath components. Path-loss factor n representing the distance dependence of the channel path-loss is calculated for various frequency centers and bandwidths. A path-gain calculation model based on the concept of seperability of distance and frequency variables is proposed and comparison to measurements is given. Furthermore, time dispersion parameters, namely mean excess delay and root mean square (r.m.s.) delay spread are examined and their dependence on transmitter-receiver antennas separation is investigated. A power law is then employed to model the relation between the number of multipath components and the r.m.s delay spread. The temporal correlation between adjacent path amplitudes is found to be negligible. A modified Saleh-Valenzuela model is invoked to describe the clustering of multipaths, where a different power decay factor is used for the rays of the first cluster as opposed to subsequent clusters. Moreover, the Weibull distribution models the small scale channel fading with a lognormally distributed shape parameter. The average values of this parameter imply severe fading conditions. Finally, simulation results of the proposed statistical model are compared to measured data demonstrating reasonable agreement.

Received 6 August 2010, Accepted 17 September 2010, Scheduled 27 September 2010
Corresponding author: A. G. Kanatas (kanatas@unipi.gr).

1. INTRODUCTION

UWB technology has been used for many decades in military and commercial communications applications. The Federal Communication Commission's (FCC) [1] power requirement of $-41.3\,\mathrm{dBm/MHz}$, or 75 nanowatts/MHz for UWB systems, categorizes them in as unintentional radiators. Such power restriction allows UWB systems to lie below the noise floor of a typical narrowband receiver and enables UWB signals to coexist with current radio services with minimal or no interference. One of the major advantages of the large bandwidth of UWB pulses is their improved channel capacity, allowing for a data rate of Gbps. However, due to the power limitation on UWB transmissions, such a high data rate is available only for short ranges, up to 10 meters. This makes UWB systems perfect candidates for short-range, high-data-rate wireless applications (WPANs). UWB communications systems are capable of working in harsh communication channels with low Signal-to-Noise ratios (SNRs) and still offering a large channel capacity. The low transmission power requires that the potential eavesdropper be very close to the transmitter in order to be able to detect the transmitted information. In addition, UWB pulses are time-modulated with codes unique to each transmitter/receiver pair, thus enhancing security of UWB transmission. Therefore, UWB systems are considered highly secure, providing low probability of intercept and detection (LPI/D) communications that is critical for military operations. Moreover, UWB systems offer high processing gain due to the ratio of the RF bandwidth to the information signal bandwidth. The resulting frequency diversity gain makes UWB signals relatively resistant to intentional and unintentional jamming. UWB systems can penetrate effectively through various materials and this property makes UWB technology viable for through-the-wall communications and ground-penetrating radars. Nevertheless, the performance of a UWB communications system may still be degraded by strong narrowband interference from coexisting radio transmitters. In addition, the phenomenon of multipath is unavoidable in wireless communications channels. Although the very short duration of UWB pulses makes them less sensitive to the multipath effect, the fading severity is of great importance to the system performance. A major application of UWB technology in military multi-crew aircrafts can be an intercommunication system attached to crewmember's helmet or headset. Several mobile users form an ad-hoc network and maintain intercommunication while performing their mission duties. Moreover, such a system is autonomous in terms of power requirements allowing for uninterrupted operation. Because of the large throughput rates achieved, the

potential services range from real-time communications to video applications, or radar systems and monitoring.

As with any electromagnetic wave, the propagation of UWB signals is governed by the properties of materials in the propagation medium. Thus, information on the electromagnetic properties of the areas where measurements have been made, provide valuable insight in appreciating the capabilities and limitations of UWB technology for indoor applications. A number of researchers [2–11] have studied UWB channel characteristics in commercial, industrial or in house environment using frequency-domain measurements. The author in [12] presents an overview of UWB propagation channels and their characteristics, summarizing the basic theory and techniques for measurements and modeling. The most popular model used to describe the tendency of multipath components (MPCs) arriving in clusters is the Saleh-Valenzuela (S-V) mathematical equation for the complex baseband impulse response [13]. Several modifications of this model have been proposed for the number of clusters, the paths inter-arrival times and the cluster decay time [14]. Furthermore, various statistical distributions have been used to model the small scale fading of the MPCs amplitudes, e.g., Nakagami, Rice, Lognormal, Weibull, Rayleigh, etc. [13–15]. In [14] the authors describe a standardized model for several typical indoor and outdoor environments. The model is based on measurement and simulation results tabulated for these environments. Recently [15], a comprehensive overview of measurements results in indoor environments was presented, providing tables with integrated survey data. In [16] the UWB radio-wave propagation within the passenger cabin of a Boeing 737–200 aircraft is investigated. The authors provide large scale channel modeling parameters, whereas in [17] they propose a pair of statistical models that describe the UWB channel impulse responses in line-of-sight (LOS) and non-line-of-sight (NLOS) conditions. The authors in [18] study the manner the human presence affects radiowave propagation within an aircraft cabin. A narrowband study [19] in a larger aircraft yields path-loss exponent values and results on fading statistics.

The objective of this work is to examine the propagation characteristics in a military cargo airplane, where the presence of numerous metallic surfaces and the absence of plastics and wood lead to a dense channel. A Lockheed C130 Hercules airplane which was parked for maintenance, at the facilities inside the Hellenic Aerospace Industry S.A. plant was chosen for this investigation. The characterization method is based on measuring the channel transfer function (CTF), and yields a number of parameters, like the path-gain (PG), the distance dependent path loss factor n, power delay

profiles (PDPs) and the number of MPCs that exist above a predefined power level, the percentage of the total energy these MPCs carry and time dispersion parameters, such as mean excess delay (m.e.d.), r.m.s. delay spread and temporal correlation between adjacent path amplitudes. A modified model is proposed for the calculation of the path-gain at specific frequencies and transmitter-receiver distance and it is compared to measurement data. The time dispersion parameters are calculated for various threshold values and an investigation of the relation of the r.m.s. delay spread to the transmit-receive antennas separation, as well as the path-loss, was performed. Subsequently, by exploiting a power law, the relation of the r.m.s. delay spread to the average number of MPCs was modeled. Another important aspect of every channel modeling activity is the investigation of the distribution function that the various channel parameters follow, offering an insight of the statistical fading behavior. In this study, a statistical–based UWB channel model is used and the clustering phenomenon of MPCs observed in the measurement results is incorporated. The model follows the Saleh-Valenzuela concepts [13], although a modification regarding the first cluster in LOS scenarios is proposed. The distribution of the path amplitudes is compared to some well-known theoretical distributions for amplitude statistics using the Kolmogorov-Smirnov (K-S) hypothesis test. The authors in [20] presented results for the path-loss characteristics for a bandwidth of 7.5 GHz with center frequency at 6.85 GHz and values for the time dispersion parameters for a threshold of -70 dB.

The remainder of the paper is organized as follows: Section 2 describes the equipment setup, the measurement and calibration procedure and the environment of the campaign. Section 3 provides the parameters estimation procedure as well as results for the distance and frequency dependent path-loss factors. These results are used to validate the proposed model for the path-gain. In Section 4 the time dispersion parameters are investigated while in Section 5 the statistical channel modeling is presented. Conclusions are drawn in Section 6.

2. MEASUREMENT SETUP, PROCEDURE AND ENVIRONMENT

Measurements were conducted in the frequency domain. The channel characterization method was based on measuring the CTF in the spectrum allocated by FCC for UWB signals i.e., 3.1 GHz to 10.6 GHz. The equipment used was a vector network analyser (VNA), a power amplifier, a pair of wideband antennas and a pair of low loss RF cables. In particular, the Agilent VNA model N5230A was used,

which is capable of sweeping the desired frequency spectrum. Also, Electrometrics EM6865 omni-directional wideband antennas with 0 dBi gain were utilized, along with a HP8449B low noise, 30 dB gain, wideband high power amplifier. The latter is characterized by constant gain over the measured frequency band and its transfer function was subtracted from the channel measurement at the calibration stage. During the measurement campaign, the VNA was set to generate 6401 continuous wave tones that were uniformly distributed over the 3.1–10.6 GHz spectrum. The frequency step was therefore equal to 1,171,875 Hz. VNA output power level during measurement procedure was +4 dBm. Figure 1 depicts the equipment setup.

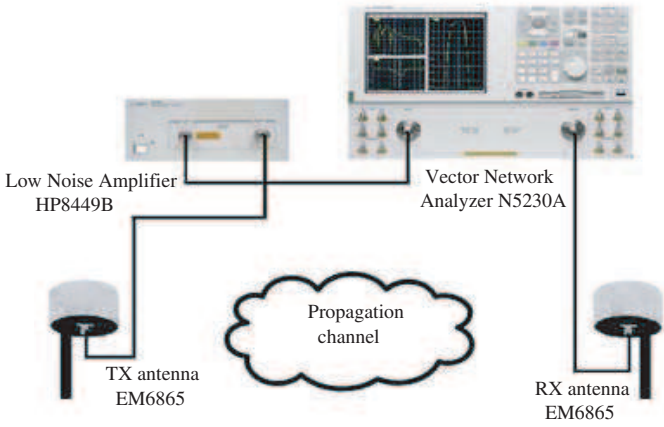

Figure 1. Overview of the equipment setup.

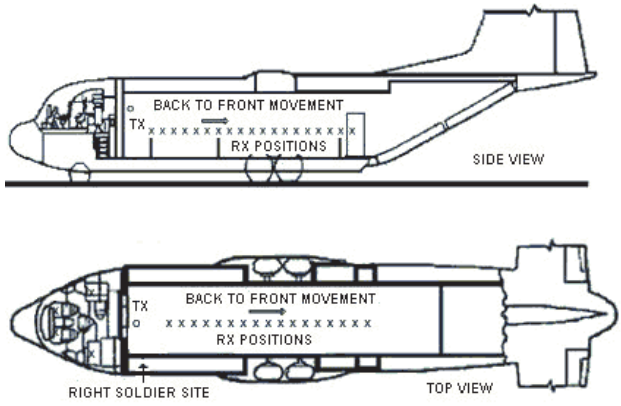

Figure 2. Sketched plan of TX(o) and RX(x) antennas.

The campaign consisted of 13 different LOS and NLOS measurement scenarios. For each scenario the transmitter was fixed and the CTF was measured for several positions of the receiver. The transmitter height was either 1.35 m or 2.5 m above the floor, according to the scenario. The receiver was mounted on a tripod at specific per scenario height of 1.35 m or 0.70 m above the floor. The measurements were taken with fixed antennas. The closest distance of the TX and RX antennas was 1 m, whereas the maximum distance was 14.5 m in the airplane body. Starting from 1m separation, the RX antenna was moved in steps of 20 cm or 40 cm, according to the scenario, providing multiple, spatially shifted static measurements. Figure 2 presents a sketched plan of the typical in-plane environment and the measurement setup for a specific scenario.

LOS measurements took place in the cargo cabin of the airplane (scenarios 1–10 of Table 1) whereas NLOS measurements were taken between crew and cargo cabin (scenarios 11–13 of Table 1). Table 1 provides the spatial characteristics of the measurement campaign. Different scenarios correspond to different locations and heights of the transmitting (TX) and the receiving (RX) antennas, as well as different spacing between measurement points. A set of 32 time snapshots of the CTF were recorded at each spatial measurement point in order to confirm the time-invariant nature of the channel and to improve the statistical analysis reliability. The recorded values of the CTFs were indexed $H(f_i, t_j; d_l)$, where $i = 1, \ldots, 6401$, $j = 1, \ldots, 32$ and l varied according to the scenario.

2.1. Calibration Issues

Prior to measurements in the airplane, equipment and cables calibration was performed in order to extract their influence from the measured data. Since the VNA measured the transfer function of the radio channel, it was necessary to remove the antenna effects and calculate the propagation CTF for further analysis. The measured radio channel transfer function is given by

$$H_{radio}(f) = \sum_{i=1}^{6401} S_{21}^{meas}(f_i)\,\delta(f - f_i), \qquad f_1 \le f \le f_{6401} \tag{1}$$

where $S_{21}^{meas}(f_i)$ is the measured S_{21} parameter by the VNA at frequency tone f_i, and 6401 frequency tones were used. This function includes the effects of both the propagation channel and the transfer functions of the transmitting and receiving antennas, i.e.,

$$H_{radio}(f) = H_{prop}(f)\,H_{Atx}(f)\,H_{Arx}(f) \tag{2}$$

Table 1. Scenarios and spatial characteristics of the measurement campaign.

Scenario, Type	TX Area of Installation, Height	RX Area of Installation, Height	RX Orientation of Movement, Step
1, LOS	back side of central corridor, 1.35 m	central corridor, 1.35 m	from back to front, 20 cm
2, LOS	front side of central corridor, 1.35 m	central corridor, 1.35 m	from front to back, 20 cm
3, LOS	back side of central corridor, 2.5 m	central corridor, 1.35 m	from back to front, 40 cm
4, LOS	back side of central corridor, 2.5 m	right soldier site, 70 cm	from back to front, 40 cm
5, LOS	front side of central corridor, 2.5 m	central corridor, 1.35 m	from front to back, 40 cm
6, LOS	front side of central corridor, 2.5 m	right soldier site, 70 cm	from front to back, 20 cm
7, LOS	middle side of central corridor, 2.5 m	right soldier site, 70 cm	from front to back, 20 cm
8, LOS	middle side of central corridor, 2.5 m	right soldier site, 70 cm	from middle to front, 20 cm
9, LOS	middle side of central corridor, 2.5 m	central corridor, 1.35 m	from front to back, 40 cm
10, LOS	middle side of central corridor, 2.5 m	central corridor, 1.35 m	from middle to front, 40 cm
11, NLOS	front side of central corridor, 2.5 m	pilots cabin, 1.35 m	inside pilots cabin, 40 cm
12, NLOS	inside pilots cabin, 1.35m	left soldier site, 70 cm	from front to back, 40 cm
13, NLOS	inside pilots cabin, 1.35 m	right soldier site, 70 cm	from front to back, 40 cm

where $H_{prop}(f)$ is the desired CTF and $H_{Atx}(f)$, $H_{Arx}(f)$ are the transfer functions of the antennas utilized. The transmitting and receiving antennas used in this campaign were vertically polarized, omnidirectional and identical, and so are the transfer functions in (2). The antenna transfer function was measured following the procedure described in [21]. The measurement was performed in the anechoic chamber using a standard antenna with transfer function $H_{std}(f)$. The

antenna under test transfer function was calculated by

$$H_A(\theta, \phi, f) = \frac{S_{21}(f)}{H_{fs}(f) H_{std}(f)} \tag{3}$$

where $S_{21}(f)$ is the VNA recording in the anechoic chamber, $H_{fs}(f) = \frac{\lambda}{4\pi d_0} e^{-j\frac{2\pi}{\lambda}d_0}$, is the free space transfer function, and d_0 is the reference distance of the measurement. The transfer function was evaluated with a step of 5° in both the azimuth and elevation angular domains, and at 6401 different frequency tones. Therefore, $36 \times 72 \times 6401$ complex values $H_A(\theta_p, \phi_q, f_i)$, $(p = 1, \ldots 36,\ q = 1, \ldots, 72,\ i = 1, \ldots 6401)$ were measured. VNA output power level during calibration procedure was +4 dBm.

Although the directional characteristics of the antenna transfer function were available in the anechoic chamber, they were ignored in order to simplify the calibration procedure. This was done by computing the average value over the horizontal plane, i.e., over the 72 azimuth samples, and over the vertical plane, i.e., over the 36 elevation samples. The propagation channel transfer function was evaluated by (2). A short discussion on the consequences of the calibration method follows. According to [12], in order to perfectly de-embed the propagation from the radio channel, i.e., to deconvolve the channel response and antennas, one should measure the frequency-dependent double-directional channel response that accounts for the angle-of-arrival (AoA) and angle-of-departure (AoD) of each MPC and the frequency-dependent three dimensional radiation pattern of each antenna. This procedure, although theoretically accurate, is practically very hard to apply, since the implementation of the required measurement setup within the cargo cabin of the airplane was very difficult. Even if antenna arrays were used to determine the directions of the MPCs, the transmitter or receiver antenna pattern in both the azimuth and elevation planes is altered with respect to the one measured in the anechoic chamber. This change is attributed to the interaction of the antenna with the nearby conductive scatterers as well as to the varying relative distance of the two antennas during the measurement. Nevertheless, the simplified deconvolution performed is reasonable for the specific measurement environment. This is due to the rich scattering conditions in the body of the C130 airplane. A very large number of MPCs arrive from all possible directions and each resolvable MPC is composed by many partial waves. Provided that the channel is adequately triggered to produce the multiplicity of the MPCs, and because the directivity of any antenna integrated over all directions would be unity for all frequencies, the propagation channel transfer function would be statistically independent of the directional

characteristics of the transmitting and receiving antennas. It should be emphasized that due to the non-uniformity of the antenna patterns, the necessary condition for this to hold is a uniform angular distribution of a large number of arriving at the receiver waves. This is a reasonable assumption for the metallic cavity where the transmitting and receiving antennas are placed in. The operation of this cavity resembles that of a reverberation chamber or a scattered field chamber producing quasi-isotropic scattering. Therefore, averaging of the antenna transfer function measured in the anechoic chamber over all angular directions for each frequency tone should be adequate for the deconvolution. The same propagation conditions were recorded in [17], supported by similar reasoning.

3. PATH-GAIN MODELING

The channel path-gain is an important parameter for link budget calculation and system design, because it determines the average signal–to-noise ratio at the receiver side. It is well-known that the wideband path-gain is a function of frequency and distance. In [8, 14] it was assumed that the distance dependent path-gain $PG(d)$ and the frequency dependent path gain $PG(f)$ can be considered to be independent so that the total path-gain $PG(f,d)$ can be written as

$$PG(f,d) = PG(f) \cdot PG(d) \tag{4}$$

where, according to [8, 14], $\sqrt{PG(f)} \propto f^{-k}$ and the distance dependence can be modelled by a conventional power law relationship, similar to narrowband channel models. In this paper, it is assumed that the total path-gain expressed in dB at a distance d and at a frequency f is given by the sum of a deterministic term and a random value as

$$\begin{aligned} PG_{dB}(f,d) &= PG_{est}(f,d) + \varepsilon \\ &= \overline{PG_{dB}}(f_c, d_0) - 10n\log_{10}\left(\frac{d}{d_0}\right) - 20k\log_{10}\left(\frac{f}{f_c}\right) + \varepsilon \end{aligned} \tag{5}$$

where $\overline{PG_{dB}}(f_c, d_0)$ is the arithmetic mean of the $\overline{PG}_{dB}(d_0)$ i.e., the average path-gain at a reference distance d_0 over all frequency bins, and the $\overline{PG}_{dB}(f_c)$ i.e., the average path-gain at the central frequency of the measurement bandwidth over all distances. The factor n is the path-loss factor expressing the distance dependence and k is the path-loss factor expressing the frequency dependence of the path-gain. The error term ε, is a random variable modelled in Section 3.2. In the following, we extract results for the values of n and evaluate the accuracy of (5).

3.1. Estimation of Path-loss Factors

The data analysis procedure for the calculation of the path-loss characteristics is provided in [20]. It is assumed that the distance dependence of the path-gain follows the log-distance model with lognormal shadowing, as in narrowband models [2, 8, 11, 14]. In order to examine the variability of the distance dependent path-loss factor over different frequency bands, the frequency spectrum was divided into the different bandwidths (BW) of 0.75, 1.5, 3 and 7.5 GHz. A set of different carriers $\left(f_c^{sub}\right)$ was associated to each of these values, as shown in Table 2, and the path-loss factor values for all these pairs of $\left(BW, f_c^{sub}\right)$ was calculated. Therefore, for each bandwidth there are several path-loss factor values that correspond to different central frequencies, e.g., for 0.75 GHz there are 10 values. Table 3 contains the average values of the corresponding path-loss factor estimated at different bandwidths.

Table 2. Frequency bandwidths and centers.

BW (GHz)	*Frequency Carrier* f_c^{sub} (GHz)
0.75	3.47 4.22 4.97 5.72 6.47 7.22 7.97 8.72 9.47 10.22
1.5	3.85 5.35 6.85 8.35 9.85
3.0	4.60 6.85 9.10
3.75	4.97 8.72
7.5	6.85

As observed from the first column of Table 3, the path-loss factor n varies between 0.20 and 1.52 with a total average value for all the campaign equal to 0.61. The average values in LOS and NLOS scenarios are 0.52 and 0.93, respectively. The general, prevailing tendency is the following: The value of n is well below 2 and in most scenarios lower than 1. This is due to the propagation in a multipath-rich environment as that in a perfectly conducting configuration found in the C130 aircraft. The numerous multipath components arrive at the receiver from all directions. Therefore, a coherent addition of arriving waves increases the received power and leads to very low path-loss factors. Similar behavior was observed in industrial environments reported in [22] where the path-loss factor was found to be equal to 1.1. In the passenger cabin campaign of [15] path-loss factor n varied between 1.7 and 2.6. Typical values for the path-loss factor that express the distance dependence range from 1.18 to 2.69 [8], 1.7

Table 3. Path-loss factor for frequency bandwidths of 0.75 GHz up to 7.5 GHz.

Scenario	$n_{7.5\,\mathrm{GHz}}$	$n_{3.75\,\mathrm{GHz}}$	$n_{3.00\,\mathrm{GHz}}$	$n_{1.50\,\mathrm{GHz}}$	$n_{0.75\,\mathrm{GHz}}$
1	0.90	0.94	0.95	0.94	0.94
2	0.85	0.87	0.92	0.90	0.89
3	0.45	0.36	0.33	0.34	0.34
4	0.66	0.64	0.66	0.65	0.66
5	0.38	0.33	0.29	0.32	0.31
6	0.20	0.19	0.16	0.14	0.16
7	0.55	0.55	0.49	0.50	0.48
8	0.43	0.42	0.36	0.37	0.35
9	0.48	0.33	0.30	0.33	0.33
10	0.26	0.27	0.28	0.29	0.29
11	0.57	0.53	0.50	0.52	0.51
12	1.52	1.49	1.54	1.50	1.49
13	0.69	0.67	0.66	0.66	0.66

to 2.6 [16], 0.6 to 1.6 [10], and 1.79 to 4.58 [14], according to the specific environment. In the review of [15] path-loss exponent values are reported for many different types of environments and scenarios, ranging from 1.4 to 4.1 for regular indoor environments.

By comparing the values in each row of Table 3, one observes that in most cases the value obtained using the 7.5 GHz bandwidth is close to the average value calculated for smaller bandwidths. Furthermore, if each scenario is examined separately, it is observed that the path-loss factor n attains its maximum value in the vicinity of the higher frequency centers. This value is increased as the frequency center moves to a higher frequency area, as expected. Exactly the opposite phenomenon occurs in the NLOS scenarios, and this is due to the behavior of the material that shadows the LOS signal. The same trend is reported in [10]. Sample data of a LOS and NLOS scenarios are tabulated on Table 4 which contains the calculated values of the corresponding path-loss factor at different central frequencies.

For the frequency dependence of the path-loss a log-frequency model with lognormal variation is assumed [20]. Theoretically, one expects that provided the antenna effects are removed, then the path loss is frequency dependent due to the fact that reflection, diffraction, material penetration and other propagation mechanisms are indeed frequency dependent. For the calculation of the path-loss

Table 4. Path-loss factor n for frequency bandwidths of 0.75 up to 7.5 GHz.

Scenario	BW (GHz)	Path-loss factor n									
L.O.S	7.50	0.90									
	3.75	0.86	1.01								
	3.00	0.84	1.03	0.98							
	1.50	0.81	0.89	1.03	0.95	1.03					
	0.75	0.80	0.83	0.85	0.95	0.99	1.08	0.96	0.95	1.09	0.94
N.L.O.S	7.50	0.69									
	3.75	0.70	0.63								
	3.00	0.70	0.65	0.64							
	1.50	0.78	0.56	0.66	0.65	0.65					
	0.75	0.82	0.74	0.52	0.61	0.69	0.58	0.60	0.70	0.65	0.65

factor k, one needs to determine how the path-gain decreases with frequency whereas the rapid variations of the path-gain in consecutive frequency samples, i.e., the frequency selectivity of the channel should be removed. Therefore, the local mean values were computed by independent frequency samples following the de-correlation procedure described in detail in [20]. Path-loss factor k varied between 1.49 and 2.08 having a total average value of all the campaign equal to 1.87. The standard deviation σ_f for all the measurements is 1.19 dB. The average value of k is 1.81 and 2.05 in LOS and NLOS scenarios respectively. The average value of its standard deviation is 1.13 dB in LOS and 1.38 dB in NLOS scenarios.

3.2. Total Path-loss Model Validation

The total path-gain, $PG_{dB}(f, d)$ given in (5) is written as a sum of a deterministic term and a random variable, ε, that represents the error with respect to the measured value. For any frequency f in the range from 3.1G Hz to 10.6 GHz and for any distance d in the Tx-Rx distance range covered in each measurement scenario, two values are compared: the measured $PG_{meas}(f, d)$ recorded by VNA and the deterministic term $PG_{est}(f, d)$. The error is calculated as the difference of the two values. The mean value of the error was found to vary between -0.23 dB and -3.03 dB, with a total average value for all the campaign equal to -1.93 dB, as shown in Table 5.

In particular, for the LOS scenarios the mean value of error was

Table 5. Mean error and standard deviation of error, applying Eq. (5).

Scenario	$\overline{PG_{dB}}(f_c, d_0)$	# of Values Compared	Mean error (dB)	std of error (dB)
1	−30.75	31 × 6401	−0.74	5.45
2	−29.55	22 × 6401	−1.13	5.57
3	−35.56	26 × 6401	−2.31	5.37
4	−37.05	27 × 6401	−1.64	5.33
5	−36.10	28 × 6401	−1.41	5.33
6	−37.35	28 × 6401	−2.23	5.44
7	−35.13	15 × 6401	−2.74	5.38
8	−35.75	15 × 6401	−1.92	5.32
9	−33.63	13 × 6401	−2.67	5.48
10	−35.11	13 × 6401	−2.90	5.41
11	−47.09	6 × 6401	−3.03	5.92
12	−49.31	28 × 6401	−0.23	5.08
13	−50.96	29 × 6401	−2.11	5.06

found to be −1.86 dB whereas for NLOS −2.07 dB. Furthermore, the standard deviation of error varied between 5.06 dB and 5.92 dB, i.e., similar values were observed in LOS and NLOS scenarios, having a total average value for all the campaign equal to 5.4 dB. The error term ε, was found to follow the smallest extreme value Type I distribution (sometimes called Gumbel distribution), the probability density function of which is given by

$$f(x) = \frac{1}{\beta} e^{\left(\frac{x-\alpha}{\beta}\right)} e^{-e^{\left(\frac{x-\alpha}{\beta}\right)}} \tag{6}$$

where α is the location parameter and β is the scale parameter of the distribution. The Gumbel distribution is appropriate for modeling the error since it is skewed to the left, i.e., there are few small values in the lower tail and many more values in the upper tail of the error values population, as shown in Figure 3.

This is justified by the fact that the deterministic term provides a smoothed estimate and the smallest extreme values are not modeled. Therefore, the deterministic term overestimates the path-gain and the smallest extreme values are incorporated by the Gumbel random variable. The location parameter of the Gumbel distribution ranges from −0.41 dB to 2.15 dB, with an average value of 0.57 dB over all

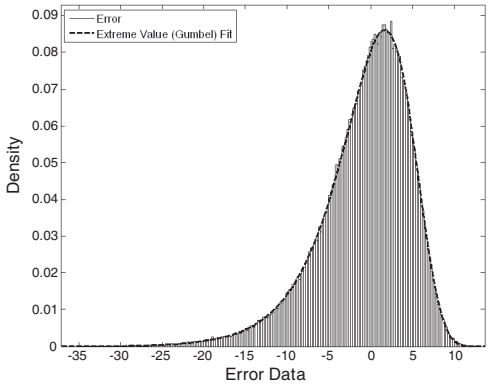

Figure 3. The empirical probability density function of the error and the corresponding fit with the Gumbel el distribution ($\alpha = 1.71$, $\beta = 4.27$) for scenario 1.

measurement scenarios. The scale parameter ranges from 4.24 dB to 5.45 dB, with an average value of 4.42 dB. Figure 3 depicts a typical empirical probability distribution function of the error and the corresponding fit with the Gumbel distribution.

4. TIME DISPERSION PARAMETERS

The discrete time impulse response was selected to model the wideband channel and the corresponding multipath components. In this model the multipath delay axis is discretized into equal slots called bins. The width of each bin is $\Delta\tau = \tau_{i+1} - \tau_i$, and is determined by the measurement resolution which in turn is dictated by the measurement bandwidth. In this measurement campaign the bandwidth swept by the VNA was 7.5 GHz and the corresponding delay bin width was 133.3 ps. All multipath components received within the ith bin are represented by a single resolvable multipath component with delay τ_i. The relative delay of the ith MPC as compared to the first arriving path is the excess delay, and, the maximum excess delay of the propagation channel is given by $N\Delta\tau$ where N is the total number of possible resolvable multipath components. The maximum value of resolvable MPCs is 6401 and the maximum value of the excess delay is 853,47 ns. The received signal consists of a series of attenuated, time-delayed and phase-shifted replicas of the transmitted signal. Assuming that the rate of the variation of amplitude and phase is slow in comparison to the measurement time interval, the involved parameters can be treated

as time-invariant random variables within a measurement period. The measured channel in the airplane was stationary and is modeled by the time-invariant channel impulse response (CIR),

$$h(\tau) = \sum_{i=0}^{N-1} a_i(\tau) e^{j\varphi_i(\tau)} \delta(\tau - \tau_i) \tag{7}$$

where $a_i(\tau)$, $\phi_i(\tau)$, τ_i are the real amplitude, the phase and the excess delay, respectively of the ith MPC. The complex baseband CIR $h(\tau, d_l)$ was calculated by inverse Fourier transform (IFFT) of the measured CTF samples $H(f_i; d_l)$. Prior to Fourier transform, an average CTF over the 32 snapshots of the CTF measured at each spatial point was calculated and Hamming windowing of the CTF samples was performed. Windowing improves the dynamic range of the time domain and produces an impulse stimulus with lower side-lobes but wider pulse width. The time dispersion modeling of the channel is based on the power delay profile (PDP).

The following processing steps were applied to the CIR. First, the CIR was normalized to its maximum value; then, the power delay profile was calculated as $P(\tau, d_l) = |h(\tau, d_l)|^2$. Next, the MPC with the maximum power was identified and located at the origin of the delay axis, whereas all MPCs were normalized in power with respect to the first MPC. It should be mentioned that in all calculated PDPs the first component was also the most significant one. The time dispersion parameters presented herein were calculated for each distance of each measurement scenario. The calculation was based on the PDPs after applying a threshold value with respect to the strongest MPC. All

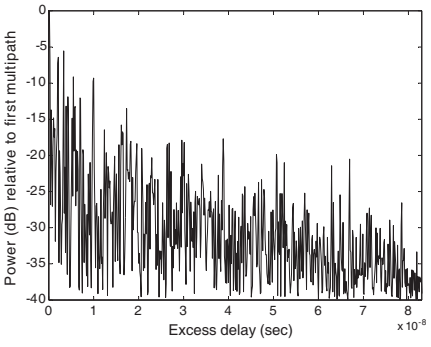

Figure 4. Local PDP of scenario 7, at RX-TX distance equal to 2.2 m, with −40 dB threshold.

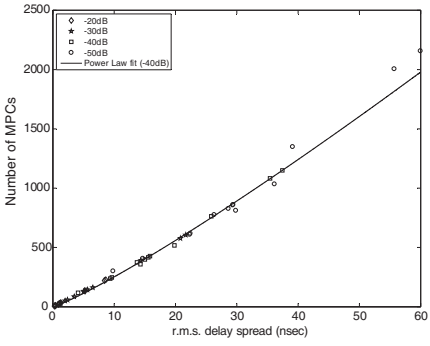

Figure 5. Power law fit of r.m.s delay spread of the campaign vs mean number of MPCs.

MPCs with power lower than the threshold value were discarded. Several threshold values were applied varying from −20 dB to −50 dB with a step of 10 dB and various parameters values are presented. The noise floor in the measurement campaign was at least 70 dB below the maximum recorded value. Figure 4 depicts an example of a local PDP calculated from measurements in scenario 7 and at a transmitter-receiver distance of 2.2 m after applying the cutoff threshold of −40 dB. The threshold value applied at the PDP limits the maximum excess delay and consequently determines the length of the cyclic prefix in a OFDM based UWB communications system.

The parameter first calculated was the number of MPCs that arrive within a cutoff threshold. In NLOS scenarios the average number of MPCs varies between 194, 525, 999 and 1837 for a threshold of −20, −30, −40, and −50 dB, respectively, while in LOS scenarios the population of MPCs decreases to 18, 96, 324, and 710 respectively. The average number of MPCs reported in [8] was 33 for LOS scenarios and 140 for NLOS scenarios for a threshold value of −20 dB, whereas for a threshold equal to −30 dB the numbers change to 153 for LOS scenarios and 468 for NLOS scenarios. In [14] the value of MPCs for −20 dB threshold varied from 15 to 228 according to the LOS type of scenario and was equal to 1442 for a NLOS scenario.

The percentage of the total energy carried by the identified MPCs was the next parameter calculated. The average percentage of energy carried by the MPCs in LOS scenarios is 87.08%, 95.89%, 99.22%, and 99.89% for threshold levels of −20, −30, −40, and −50 dB whereas in NLOS scenarios the percentage values increases to 87.94%, 98.14%, 99.7%, and 99.95%, respectively. The large percentage values indicate that a −40 dB or even a −30 dB threshold is sufficient to compute reliable estimates of time dispersion parameters. The same trend appears in [14, 17].

In the following the time dispersion parameters for all threshold values are calculated. The mean excess delay (m.e.d.) τ_m, is defined as the first moment of PDP. The r.m.s. delay spread (r.m.s.d.s.) τ_{rms} is the square root of the second central moment of PDP,

$$\tau_m = \frac{\sum\limits_i a_i^2 \tau_i}{\sum\limits_i a_i^2} = \frac{\sum\limits_i P(\tau_i)\tau_i}{\sum\limits_i P(\tau_i)} \tag{8}$$

$$\tau_{rms} = \sqrt{\overline{\tau^2} - \tau_m^2}, \quad \overline{\tau^2} = \frac{\sum\limits_i a_i^2 \tau_i^2}{\sum\limits_i a_i^2} = \frac{\sum\limits_i P(\tau_i)\tau_i^2}{\sum\limits_i P(\tau_i)} \tag{9}$$

The average values of the mean excess delay of all the campaign is 32.6, 20.1, 9.6, and 3.4 ns, for −50, −40, −30, and −20 dB

thresholds, whereas the average values of r.m.s. delay spread of all the campaign is 31.1 ns, 17.0 ns, 7.3 ns, and 2.3 ns for the same thresholds. As the threshold ranges from −50 dB to −20 dB, the values of all time dispersion parameters decrease. The preliminary results presented in [20] were calculated for a threshold value of −70 dB. In all measurement scenarios as the distance between TX and RX antennas increases, the value of all time dispersion parameters increases too. The same trend was observed in [22], and in [23–25]. Typical values of the r.m.s. delay spread recorded in industrial environments range from 28 to 31ns for LOS scenarios and 34 to 40 ns for NLOS scenarios [22]. Measurements in high-rise apartment environments [26] have showed that the mean r.m.s. delay spread ranges from 10.36 to 45.55 ns for 4-bedroom apartments. Table 6 presents the average values of the time parameters, the number of MPCs and the energy they carry for LOS, NLOS and all the campaign scenarios respectively.

Table 6. Time dispersion parameters of the campaign.

Scenario	Parameter	Threshold			
		−50 dB	−40 dB	−30 dB	−20 dB
L.O.S	Energy %	99.89	99.22	95.89	87.08
	MPCs	710	324	96	18
	m.e.d.	26.05 ns	13.90 ns	4.54 ns	0.99 ns
	r.m.s.d.s.	24.89 ns	12.28 ns	3.78 ns	0.72 ns
N.L.O.S	Energy %	99.95	99.7	98.14	87.94
	MPCs	1837	999	525	194
	m.e.d.	54.24 ns	40.74 ns	26.61 ns	11.45 ns
	r.m.s.d.s.	51.58 ns	32.90 ns	18.954 ns	7.42 ns
Campaign	Energy %	99.9	99.33	96.41	87.27
	MPCs	971	479	195	58
	m.e.d.	32.56 ns	20.09 ns	9.63 ns	3.41 ns
	r.m.s.d.s.	31.05 ns	17.04 ns	7.28 ns	2.27 ns

The fine measurement delay resolution imposes a requirement for a large number of RAKE fingers. A partial-RAKE receiver structure that collects the energy from the first MPCs in the PDP is more appropriate for this dense channel.

The number of fingers required to capture more than the 90% of the energy is several hundred.In the following, the relation of the number of MPCs and r.m.s. delay spread is examined. It is observed

Table 7. Power law exponents for the relation of the number of MPCs with r.m.s delay spread.

Threshold (dB)	$b1$ (LOS)	$b2$ (NLOS)	c (Campaign)
-50	1.14	1.03	1.27
-40	1.14	1.08	1.15
-30	1.09	1.04	1.06
-20	1.02	1.04	1.04

that the number of MPCs increases with r.m.s delay spread and a power law, of the form $N \propto \tau_{rmsLOS}^{b1}$ and $N \propto \tau_{rmsNLOS}^{b2}$ can be applied to LOS and NLOS scenarios respectively.

Typical values of the exponents $b1$, $b2$ for a LOS and a NLOS scenario are given in Table 7. Next, the relation between the average number of MPCs, $\bar{N}$ over all static measurements in all scenarios and the corresponding average r.m.s. delay spread in the C130 airplane is investigated. The trend is the same as shown in Figure 5 and a power law as, $\bar{N} \propto \bar{\tau}_{rms}^{c}$ can be used. The values of the exponent c for all threshold values are tabulated in Table 7.

Next, the dependence of r.m.s. delay spread on TX-RX distance is investigated. It is observed that r.m.s. delay spread increases with distance, or equivalently r.m.s. delay spread and path loss increase jointly. This is depicted in Figure 6, where measurement results from

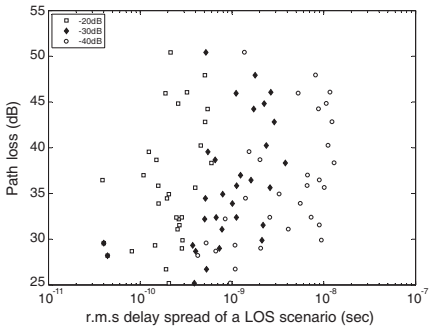

Figure 6. Path-loss versus r.m.s. delay spread in a LOS scenario.

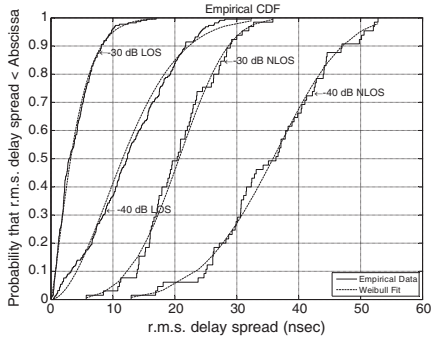

Figure 7. Cumulative distribution function of r.m.s delay spread of the campaign for -30 dB and -40 dB thresholds.

various spatial positions are shown for a LOS scenario. The same trend appears in [2]. The cdf curves of r.m.s delay spread of all measured LOS and NLOS scenarios for −30 dB and −40 dB threshold values are depicted in Figure 7. It is observed that the Weibull distribution adequately fits the empirical data. The values of the Weibull parameters a, b are given in Table 8.

Table 8. Weibull r.m.s delay spread fitting parameters for two threshold values.

Scenario Type	Distribution	Threshold	
		−30 dB	−40 dB
LOS	Weibull	$a = 4.25$	$a = 14.12$
		$b = 1.28$	$b = 1.83$
NLOS	Weibull	$a = 22.85$	$a = 38.93$
		$b = 3.68$	$b = 4.43$

4.1. Temporal Correlation

The temporal correlation between adjacent MPC amplitudes in a PDP was estimated using spatial averaging. The temporal correlation coefficient is defined as

$$\rho_{a_{k,k+1}} = \frac{E\left\{\left(a_k - \bar{a}_k\right)\left(a_{k+1} - \bar{a}_{k+1}\right)\right\}}{\sqrt{E\left\{\left(a_k - \bar{a}_k\right)^2\left(a_{k+1} - \bar{a}_{k+1}\right)^2\right\}}} \tag{10}$$

where, a_k and a_{k+1} are the amplitude of the kth and the $(k+1)$th bin respectively and $\bar{a}_k$ and $\bar{a}_{k+1}$ are the corresponding spatially averaged values. For each scenario the value of $\rho_{a_{k,k+1}}$ was calculated for all possible values of k, i.e., for all adjacent bins. The mean value over these delay taps and over all measurement scenarios was then found to be less than 0.15. This implies that the temporal correlation effect is negligible. Although this observation is in conflict with the anticipated behavior in indoor environments [12], it is reasonable since a large number of scattering objects are uniformly distributed in the airplane and therefore, different MPCs correspond to different and resolvable scatterers that result in a low degree of correlation. In the passenger cabin campaign of [17] the mean value of the temporal correlation for the different delay taps was found to be equal to 0.13. Similar results were recorded in [15, 27, 28].

5. STATISTICAL MODELING

Many channel investigations [8, 12, 14, 21, 28], have concluded that the MPCs have the tendency to arrive in multiple clusters following, with some modifications, the well-known Saleh-Valenzuela (S-V) model [13]. In [27] the authors propose the single cluster approach with exponential delay profile, whereas in [29] an exponential-lognormal model as a variation of the single cluster approach was postulated. In [30] the authors compare the three models and highlight the pros and cons for each. In this paper the authors selected the S-V model to characterize the clustering phenomenon and evidence supporting this choice is provided in this Section. The S-V model assumes that

$$h(\tau) = \sum_{l=0}^{L} \sum_{k=0}^{K_l} a_{k,l} \exp\left(j\varphi_{k,l}\right) \delta\left(\tau - \mathrm{T}_l - \tau_{k,l}\right) \tag{11}$$

where $a_{k,l}$ is the multipath gain coefficient of the kth multipath component in the lth cluster, T_l is the delay of the lth cluster i.e., the time of arrival (TOA) of the first arriving MPC within the lth cluster, and $\tau_{k,l}$ is the delay of the kth MPC relative to the lth cluster arrival time T_l. The phases $\phi_{k,l}$ are uniformly distributed in $[0, 2\pi]$. K_l is the number of rays within the lth cluster and L is the number of clusters that depends mainly on the measurement bandwidth and on the specific environment. The profiles used for the S-V model parameter extraction were calculated as an average of local PDPs measured at several distances in a measurement scenario. Therefore, a single APDP is used for each scenario. The model parameters were estimated after a threshold of $-40\,\mathrm{dB}$ was applied to the resulting APDP. Figure 8 depicts the APDP of a LOS scenario without applying any cutoff threshold, whereas Figure 9 depicts the same APDP after applying the cutoff threshold of $-40\,\mathrm{dB}$. The model parameter values are strongly dependent on the threshold value. The number of clusters, as well as the tendency the power is decaying with, greatly varies with the selected threshold. This explains, in the first place, the different structures of the models proposed in the literature. In this paper the threshold value of $-40\,\mathrm{dB}$ was adopted because the energy carried by the rays included in this window approaches 99% of the total energy in the APDP.

The first task of every statistical channel modeling procedure is to identify the clusters. It is apparent that the position and the size of clusters depend on the specific structure of the measurement campaign environment. The cluster identification employs statistical techniques. The automatic identification of the cluster regions is a very difficult procedure with questionable results and thus it is common for clusters

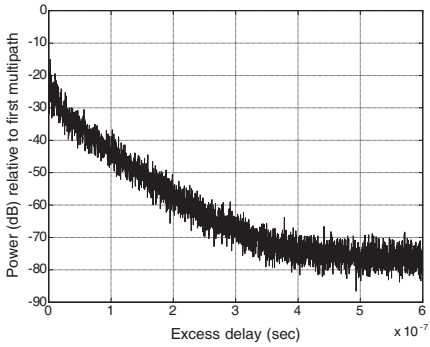

Figure 8. Typical time averaged power delay profile (APDP) of a LOS scenario without any threshold.

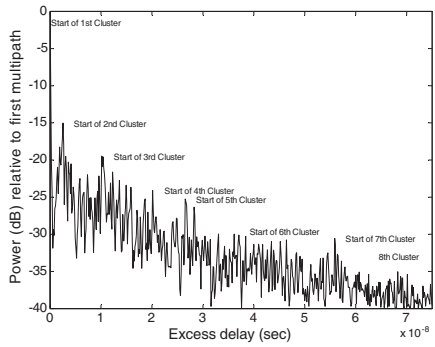

Figure 9. Typical APDP of a LOS scenario with −40 dB threshold.

to be identified by eye inspection. This procedure was followed in this work also. The onset of a new cluster was marked by a sudden and pronounced step in the received power. Each cluster was defined from the time of arrival (TOA) of its first arriving MPC and the amplitude of this first MPC was the peak amplitude of the cluster. From Figure 9 one can determine 7 different clusters.

It was observed that in LOS scenarios the number of clusters varied from 7 to 14, while in NLOS scenarios the number of clusters varied from 16 to 18. In [2] the researchers measured only one cluster in an indoor environment campaign, using a bandwidth of 1.25 GHz around a frequency center of 5 GHz, while in [28] 1 to 6 clusters were identified in LOS scenarios and 1 to 8 clusters in NLOS apartments. In [4] up to 14 clusters were reported. In the industrial environment investigated in [21] 4 to 6 clusters where reported. The increased number of clusters found in this campaign is due to the dense metallic environment of the C130 airplane. Large average number of clusters are also given in [14] for outdoor channels. In the passenger cabin campaign of [17] the shape of the PDP generally follows the single cluster model with one or more spikes within 30ns of the leading edge of response.

5.1. Mean Cluster Arrival Rate Λ and Cluster Exponential Decay Factor Γ Estimation.

According to the S-V model the cluster inter-arrival time is described by the exponential probability density function (pdf) given by:

$$p\left(T_l|T_{(l-1)}\right) = \Lambda \exp\left[-\Lambda\left(T_l - T_{(l-1)}\right)\right], \qquad l > 0 \qquad (12)$$

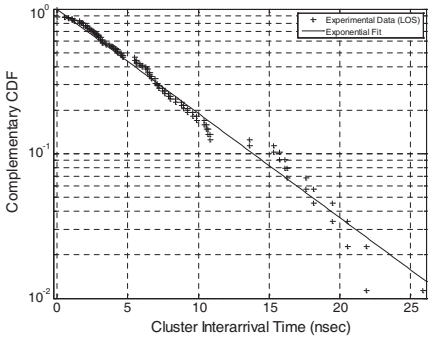

Figure 10. Cluster inter-arrival times and best exponential fit for LOS scenarios.

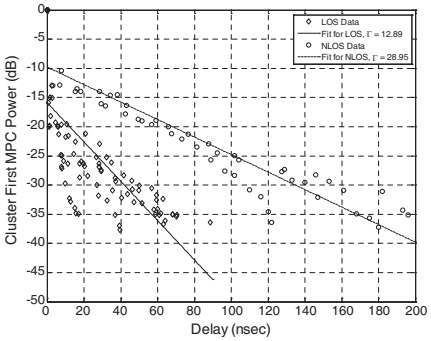

Figure 11. Estimation of cluster exponential decay factor Γ.

where Λ is the mean cluster arrival rate. Λ, T_l, l are classified as inter-cluster parameters. For the estimation of the mean cluster arrival rate Λ the following procedure was followed: The cluster arrival rate Λ was computed by measuring the cluster inter-arrival times $\Delta T_l = T_l - T_{l-1}$ for each APDP, with $\Lambda = 1/\overline{\Delta T_l}$ where $\overline{\Delta T_l}$ is the average value over all l within every APDP. The value of cluster arrival rate $1/\Lambda$ was found to be 6.02 ns for the LOS scenarios and 9.95 ns for the NLOS scenarios, respectively. Figure 10 presents the complementary cdf of the cluster inter-arrival times and the corresponding best exponential fit for all LOS scenarios.

Having identified all the clusters of the campaign one may calculate the decay exponent of the clusters Γ. The value of Γ is determined from the best fit regression line of the first multipath component amplitude of each cluster. The decay factor is calculated as $\Gamma = \frac{10}{m_\Gamma \ln 10}$, where m_Γ is the negative slope of the regression line on the dB scale. Figure 11 depicts the cluster relative power versus the delay for all the LOS and NLOS scenarios of the campaign and also the regression line fit of the power of the LOS and NLOS scenarios of the campaign. The estimated values of the cluster exponential decay factor Γ was 12.89 ns and 28.95 ns for LOS and NLOS scenarios respectively.

5.2. Mean Ray Arrival Rate λ and Ray Exponential Decay Factor γ Estimation.

A number of different models have been proposed for the rays' inter arrival times within a cluster such as the regularly spaced arrival times [22, 27], the Poisson arrival times [13], and the mixed Poisson

process [28]. The dense metallic environment of the C130 airplane produces a very large number of multi-path components. As it is impossible to resolve the energy of each multi-path arrival by an inverse Fourier transform of the measured data we used the tapped delay line approach, i.e., every delay tap contains energy. As explained in Section 4, all multipath components received within a bin are represented by a single resolvable multipath component with the same delay. In this way, the regularly spaced arrival time model is adopted in this work and the ray arrival rate is equal to the bin duration i.e., $\lambda = 133.3$ ps.

By thorough examination of the APDPs from all LOS scenarios, it was observed that the power decay in the first cluster was different from the decay in subsequent clusters. If one calculates a common γ value for all clusters, then the resulting value would overestimate the power of rays in the first cluster. Therefore, we decided to use two different values for the power decay factor γ, one for the first cluster denoted γ_0 and one for the subsequent clusters. This applies only to LOS scenarios. Due to the limited measurement data in NLOS scenarios the reliability of a similar model would be questionable for NLOS environments. In order to estimate the decay exponent γ of the rays of the LOS and NLOS scenarios, the values of the normalized power of the rays of all LOS and NLOS scenarios and their relative delays were superimposed and plotted. Then, the method described for the estimation of the decay exponent of the clusters Γ was followed and the decay exponent of the rays of LOS and NLOS scenario was estimated as $\gamma = \frac{10}{m_\gamma \ln 10}$, where m_γ is the negative slope of the regression line on the dB scale. A similar procedure was followed for the γ_0 factor considering the rays only from the first cluster. The value of the ray exponential decay factor γ_0 is 0.54 ns for LOS, whereas the value of γ is 31.02 ns and 35.95 ns for LOS and NLOS scenarios, respectively. The regression line fitting of the power of rays of LOS scenarios is depicted in Figure 12. Table 9 summarizes the modified S-V model parameters of the campaign.

Table 9. Modified Saleh-Valenzuela parameters of the campaign.

scenarios	Γ (ns)	γ_0 (ns)	γ (ns)	$1/\Lambda$ (ns)	Clusters
LOS	12.89	0.54	31.02	6.02	8.8
NLOS	28.95	N.A.	35.95	9.95	16.7

Typical values of cluster arrival rate ($1/\Lambda$) found in literature range from 8.69 to 11.79 ns for LOS scenarios in high-rise

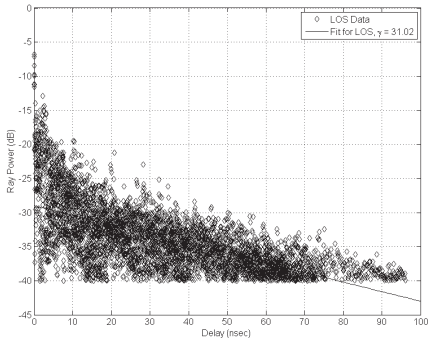

Figure 12. Estimation of ray exponential decay factor γ for LOS scenarios.

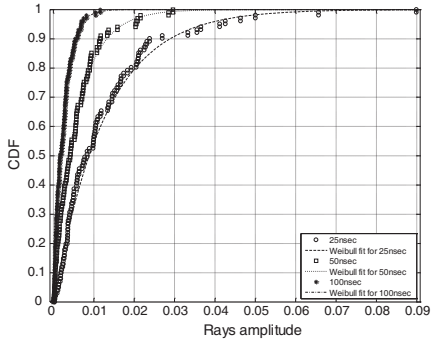

Figure 13. CDF plot of the amplitude of rays in a LOS scenario at specific time delays.

apartments [28], 21.28 ns in residential areas [14], and 15.83 ns in industrial LOS environments [22]. For NLOS cases the reported values range from 15.65 to 21.45 ns [28], and from 12.53 to 16.00 ns [21]. In [14] a typical value reported is 8.33 ns. Typical values of clusters exponential decay factor Γ range from 22.1 to 51.47 ns [28], and from 12.62 to 29.78 ns [22]. The value of Γ reported in [14] is 22.61 ns for LOS scenarios and 26.27 ns for NLOS scenarios. Typical values of rays exponential decay factor γ range from 14.27 to 38.62 ns [28], and from 12.53 to 17.50 ns [14], whereas in [22] a different γ value was considered for each cluster.

5.3. Distribution of MPCs Amplitude.

Many UWB measurement campaigns [5, 21, 27, 28, 31] for indoor channels have reported small-scale amplitude fading statistics that follow various distributions e.g., Nakagami, Rayleigh, Rice and Weibull. The scope of this subsection is to investigate which of the most frequently reported distributions fit the measured data of this campaign. Three LOS and two NLOS scenarios were chosen for the small-scale fading characterization. The data values used for this purpose are acquired using a 1 cm measurement step. The CTF was recorded at 100 consecutive spatial points and the same processing steps given in Section 4 were followed to produce the power delay profile. Setting a threshold value of -40 dB in power, the remaining non-zero amplitudes of the delay bins in the channel impulse response were selected. The amplitude values that correspond to the same delay bin were collected and formed a data vector, the distribution of

Table 10. Passing rate of the K-S test.

Scenario	Lognormal	Nakagami	Rayleigh	Rice	Weibull
A (LOS)	87.2	92.1	0.4	0.5	99.9
B (LOS)	96.1	96.4	3.3	3.3	99.9
C (LOS)	96.4	95.7	2.8	2.9	99.7
D (NLOS)	87.7	85.0	0.1	0.1	99.8
E (NLOS)	92.4	80.7	0.1	0.1	99.7

which was compared to a hypothesized distribution. The Kolmogorov-Smirnov (K-S) hypothesis test was used to determine the fitting effectiveness of the hypothesized distributions at 5% significance level. The null hypothesis for the K-S test is that the amplitude follows a predefined distribution. The result of the test is a logic one if one can reject the hypothesis that the amplitude follows the hypothesized distribution and logic zero otherwise. The test was performed to all delay bins and for all distributions shown in Table 10. The percentage values shown in this table correspond to the percentage of delay bins for which the result of the test was a logic zero and therefore the population distribution from which the data sample is drawn conforms to the hypothesized distribution. This percentage value is called passing rate of the K-S test for the specific distribution.

Observing the passing rates one may conclude that the Weibull distribution has the highest passing rate in all the different scenarios of the campaign. The same trend appears in [28, 31, 32]. The question that arises is related to the poor fitting results of Rayleigh and Rice distributions given that a large number of MPCs are present in the body of the airplane. Rayleigh distribution is used to describe the short-term signal amplitude variation under the assumption of homogeneous diffuse scattering field, resulting from randomly distributed point scatterers around the receiver. In particular, assuming [33] a large number of partial waves, identical partial wave amplitudes, no correlation between different partial waves, no correlation between phase and amplitude of one partial wave, and uniform phase distribution on $[0, 2\pi]$, the central limit theorem leads to a complex Gaussian distribution for the complex envelope. Therefore, if $h = x + jy = re^{j\varphi}$ models the complex Gaussian process, x, y are Gaussian-distributed variables with zero mean and equal variance. This implies Rayleigh distribution of the envelope that changes to Rice distribution if a strong constant amplitude is

superimposed. In [34] it was clearly stated that the phase correlations of the partial waves due to the scattering from the spatially correlated surface make the assumption of a homogeneous phase distribution invalid, resulting in different amplitude distributions. The spatially correlated surface implies a non-linear propagation environment [35]. The resulting envelope is obtained as a nonlinear function of the modulus of the process h. The non-linearity is manifested in terms of a power parameter $b > 0$, such that the envelope $r = |h|$ can be expressed as a power transformation of a Rayleigh distributed random variable. For the Weibull fading model, the complex envelope can be written as a function of the Gaussian in-phase and quadrature components $h = (x + jy)^{2/b}$. If $z = |x + jy|$ is Rayleigh distributed, then $r = z^{2/b}$ is Weibull distributed

$$f(r) = \frac{b}{a^b} r^{b-1} \exp\left(-\frac{r^b}{a^b}\right) \tag{13}$$

where $a^b = E\left\{r^b\right\}$ is the average fading power and b expresses the fading severity ($b > 0$). As b increases the fading severity decreases and for $b = 2$ reduces to Rayleigh distribution. In the propagation environment of the military airplane under investigation, the applicability of the Weibull distribution is justified as follows: the received complex envelope in each delay bin is a summation of a large number of coherently scattered waves. This happens since the bandwidth used is large (7.5 GHz) and the corresponding delay resolution is fine (133.3 psec). Therefore, the partial waves arriving in each delay bin originate from scattering from smooth and thus spatially correlated surfaces, and the phases of these waves are correlated. This leads to non-linear propagation environment and the Weibull distribution of the envelope is a reasonable choice. Figure 13 depicts the cdf of the MPCs amplitudes of a LOS scenario for the time delay bins of 25 nsec, 50 nsec and 100 nsec respectively. The continuous lines correspond to the Weibull distribution used to fit the empirical data with parameters (a, b) given by (0.013, 1.01), (0.006, 0.96) and (0.002, 1.04) respectively for the three bins. The estimated parameters (a, b) of the Weibull distribution for all examined scenarios are random values. Indeed, the b-shape parameter was found to follow the lognormal distribution with mean, μ_b and standard deviation, σ_b given in Table 11. The same behavior was reported in [28]. It was observed that in NLOS environments the b-shape parameter is smaller than in LOS scenarios and therefore the fading phenomenon is more severe, leading to worse probability of error performance. Moreover, the mean value of the b-shape parameter is close to one, implying worse than Rayleigh fading conditions. This result implies that diversity schemes

are required to provide a steep slope of the BER-vs-SNR curve. In the passenger cabin campaign of [17], the small scale fading of the MPCs tends to follow a Nakagami distribution with a lognormally-distributed m parameter that is close to 0 dB which corresponds to Rayleigh fading with small variance.

Table 11. Mean and standard deviation of lognormal distributed Weibull b-shape parameter.

Scenario	Mean, μ_b	Standard Deviation, σ_b
A (LOS)	0.02	0.1
B (LOS)	0	0.1
C (LOS)	−0.01	0.1
D (NLOS)	−0.18	0.1
E (NLOS)	-0.18	0.1

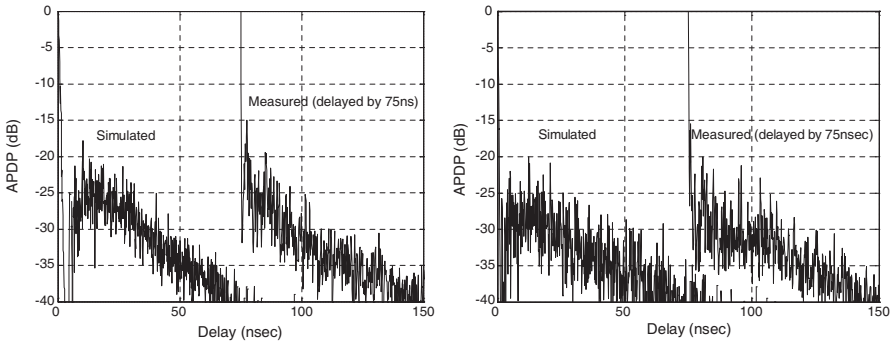

(a) Scenatio 7 LOS (b) Scenario 8 LOS

Figure 14. Comparison of measured and simulated APDPs.

5.4. Simulation of Power Delay Profiles

In order to assess the validity of the proposed model and verify that the channel simulator produces convincing results, an ensemble of PDPs were generated using parameters extracted from specific LOS scenarios. The comparison to the measurement results is based on the form of the APDPs as well as the cdf of the r.m.s. delay spread. Although these criteria do not ensure that the regenerated PDPs yield the same link performance results with the measured PDPs [30], they

provide an indication on the resemblance of the statistical properties. Figure 14 presents the comparison of measured and simulated APDPs for parameters extracted from two LOS scenarios. The two profiles compare well. Figure 15 presents the cdf of the the r.m.s. delay spread for all the LOS scenarios. One observes that the measured data preserve greater variance. This is expected since the measured data are calculated from different spatial positions of the LOS scenarios.

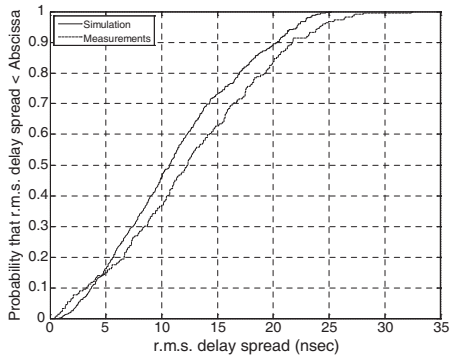

Figure 15. Comparison of the cdf plot of measured and simulated r.m.s. delay spread.

6. CONCLUSION

This paper presented results obtained from an UWB measurement campaign in a Hercules C130 military cargo airplane. The main conclusions drawn from the investigation are the following: The path-loss factor n increases with the carrier frequency, is well below 2 and in most cases below 1. This is due to the propagation in the multipath-rich environment of the C130 aircraft and offers the capability to extend the range of the system. The sub-bands undergo different attenuation and this cannot be resolved by increasing the power of specific higher frequencies. Thus, either new modulation and coding schemes, or division of the available frequency band into sub-bands is required. Using these empirical results for n, k the accuracy of the proposed model for the path-gain calculation was calculated. The path-gain is written as a sum of a deterministic term and a random variable that represents the error with respect to the measured value. This error follows the Gumbel distribution. In all measurement scenarios as the TX-RX distance increases the value of all time dispersion parameters increases too. The cutoff threshold of -20, -30, -40, and $-50\,\mathrm{dB}$

below the strongest path in each PDP determines the amount of energy and the population of MPCs. The number of multipath components is greater in NLOS scenarios. The number of MPCs is well above the values presented in the literature due to the conductive cavity of the military airplane. In all scenarios, as the threshold moves from −50 dB to −20 dB, the values of all time dispersion parameters decrease. These values tend to increase with the TX-RX distance in LOS environments. The threshold value applied at the PDP limits the maximum excess delay and determines the length of the cyclic prefix in a OFDM based UWB communications system. A power law was employed to model the relation between the number of MPCs and the r.m.s. delay spread. An increase in r.m.s. delay spread was observed with increasing path-loss. The temporal correlation effect in the airplane's environment is negligible because the scattering objects are uniformly distributed. A modified S-V model was used to describe the clusters and rays in the spatially averaged PDP of each measurement scenario. The proposed modification refers to the different decay factor of the power of rays in the first cluster as compared to subsequent clusters. Moreover, the best fit to the amplitude distribution of the MPCs was found to be the Weibull distribution. The number of clusters identified in all scenarios is large. The increased number of multipath components in the examined environment leads to a dense channel providing increased energy at the receiver but with severe fading, since the b-shape parameter of the Weibull distribution is close to one, implying worse than Rayleigh fading conditions. Therefore, diversity schemes are required to provide a steep slope of the BER-vs-SNR curve. Finally, a partial-RAKE receiver structure that collects the energy from the first MPCs in the PDP is more appropriate for this dense channel. The number of fingers required to capture more than the 90% of the energy is several hundred.

ACKNOWLEDGMENT

The authors wish to thank Hellenic Aerospace Industry S. A for providing the research environment, the electronic equipment, and the Hercules C130.

REFERENCES

1. Federal Communication Commission, First Report and Order, FCC 02-48, 12, April 2002.
2. Ghassemzadeh, S. S., R. Jana, C. Rice, W. Turin, and V. Tarokh, "Measurement and Modeling of an ultra-wide bandwidth indoor

channel," *IEEE Trans. on Commun.*, Vol. 52, No. 10, 1786–1796, 2004.

3. Prettie, C., D. Cheung, L. Rusch, and M. Ho, "Spatial correlation of UWB signals in a home environment," *IEEE Conf. on Ultra Wideband Systems and Technologies*, 65–69, May 2002.
4. Keignart, J., C. Abou-Rjeily, C. Delaveaud, and N. Daniele, "UWB SIMO channel measurements and simulation," *IEEE Trans. Microwave Theory and Techniques*, Vol. 54, No. 4, 1812–1819, Jun. 2006
5. Kunisch, J. and J. Pamp, "Measurement results and modeling aspects for the UWB radio channel," *IEEE Conf. on Ultra Wideband Systems and Technologies*, 19–23, May 2002.
6. Street, A., L. Lukama, and D. Edwards, "Use of VNAs for wideband propagation measurements," *IEE Proc.*, Vol. 148, No. 6, 411–415, Dec. 2001.
7. Hovinen, V., M. Hämäläinen, and T. Pätsi, "Ultra wideband indoor radio channel models: Preliminary results," *IEEE Conf. on Ultra Wideband Systems and Technologies*, 75–79, May 2002.
8. Chong, C. C., Y. E. Kim, S. K. Yong, and S. S. Lee, "Statistical characterization of the UWB propagation channel in indoor residential environment," *Wiley J. Wireless Commun. Mobile Computing*, Vol. 5, No. 5, 503–512, Aug. 2005.
9. Alvarez, A., G. Valera, M. Lobeira, R. Torres, and J. L. Garcia, "Ultra wideband channel model for indoor environments," *Journal of Commun. Networks*, Vol. 5, No. 4, 309–318, Dec. 2003.
10. Cassioli, D., A. Durantini, and W. Ciccognani, "The role of path loss on the selection of the operating bands of UWB systems," *Proc. IEEE Int. Symp. on Personal, Indoor and Mobile Radio Communications*, Vol. 4, 2787–2791, Barcelona, Spain, Sep. 2004.
11. Buehrer, R., W. Davis, A. Safaai-Jazi, and D. Sweeney, "Ultra-wideband propagation measurements and modeling," DARPA NETEX Final Technical Report, Jan. 2004.
12. Molisch, A. F., "Ultrawideband propagation channels-theory, measurements and modeling," *IEEE Transactions on Vehicular Technology*, Vol. 54, No. 5, 1528–1545, Sep. 2005.
13. Saleh, A. and R. A. Valenzuela, "A statistical model for indoor multipath propagation," *IEEE J. Sel. Areas Commun.*, Vol. 5, No. 2, 128–137, Feb. 1987.
14. Molisch, A. F., D. Cassioli, C. C. Chong, S. Emami, A. Fort, B. Kannan, J. Karedal, J. Kunisch, H. G. Schantz, K. Siwiak, and M. Z. Win., "A comprehensive standardized model for UWB

propagation channels," *IEEE Trans. Antennas and Propagation*, Vol. 54, No. 11, 3151–3166, 2006.

15. Ahmadi-Shokouh. J. and R. C. Qiu, "Ultra-wideband (UWB) communications channel measurements — A tutorial review," *Int. J. Ultra Wideband Communications and Systems*, Vol. 1, No. 1, 11–31, 2009.
16. Chuang, J., N. Xin, H. Huang, S. Chiu, and D. G. Michelson, "UWB radio wave propagation within the passenger cabin of a boeing 737–200 aircraft," *Proc. 65th IEEE Veh. Tech. Conf., VTC2007-Spring*, 496–500, Apr. 22–25, 2007.
17. Chiu, S., J. Chuang, and D. G. Michelson, "Characterization of UWB channel impulse responses within the passenger cabin of a boeing 737–200 aircraft," *IEEE Trans on Antennas and Propagation*, Vol. 58, No. 3, 935–945, Mar. 2010.
18. Chiu, S. and D. G. Michelson, "Effect of human presence on UWB radiowave propagation within the passenger cabin of a midsize airliner," *IEEE Trans on Antennas and Propagation*, Vol. 58, No. 3, 917–926, Mar. 2010.
19. Kaouris, A., M. Zaras, M. Revithi, N. Moraitis, and P. Constantinou, "Propagation measurements inside a B737 aircraft for in-cabin wireless networks," *Proc. IEEE VTC2008-Spring*, 2932–2936, May 11–14, 2008.
20. Spiliotopoulos, C. and A. G. Kanatas, "Path-loss and time-dispersion parameters of UWB signals in a military airplane," *IEEE Antennas and Wireless Propagation Letters*, Vol. 8, 790–793, 2009.
21. Promwong, S., W. Hachitani, and J.-I. Takada, "Free space link budget evaluation of UWB-IR systems," *International Workshop on Ultra Wideband Systems 2004, Joint with Conference on Ultrawideband Systems and Technologies*, 312–316, May 18–21, 2004.
22. Karedal, J., S. Wyne, P. Almers, F. Tufvesson, and A. F. Molisch, "A measurement-based statistical model for industrial ultra-wideband channels," *IEEE Trans. on Wireless Commun.*, Vol. 6, No. 8, 3028–3037, Aug. 2007.
23. Porrat, D. and Y. Serfaty, "Sub-band analysis of NLOS indoor channel responses," *Proc. IEEE PIMRC2008*, 1–5, Sep. 15–18, 2008.
24. Qiu, R. C. and I. Lu, "Multipath resolving with frequency dependence for broadband wireless channel modeling," *Proc. IEEE Int. Conf. Commun.*, 277–281, Dallas, TX, Jun. 1996.

25. Siwiak, K., H. L. Bertoni, and S. M. Yano, "Relation between multipath and wave propagation attenuation," *IEE Electronic Letters*, Vol. 39, 142–143, Jan. 2003.
26. Chong, C., Y. Kim, and S. Lee, "UWB Indoor propagation channel measurements and data analysis in various types of high-rise apartments," *Proc. IEEE Veh. Tech. Conf., VTC2004-Fall*, 2004.
27. Cassioli, D., M. Z. Win, and A. F. Molisch, "The ultra-wide bandwidth indoor channel: From statistical model to simulations," *IEEE J. Sel. Areas Commun.*, Vol. 20, No. 6, 1247–1257, 2002.
28. Chong, C. and S. K. Yong, "A generic statistical-based UWB channel model for high-rise apartments," *IEEE Trans on Antennas and Propagation*, Vol. 53, No 8, 2389–2399, Aug. 2005.
29. Ghassemzadeh, S. S., L. J. Greenstein, T. Sveinsson, and V. Tarokh, "UWB delay profile models for residential and commercial indoor environments," *IEEE Trans. on Vehicular Technology*, Vol. 54, No. 4, 1235–1244, Jul. 2005.
30. Greenstein, L. J., S. S. Ghassemzadeh, S.-C. Hong, and V. Tarokh, "Comparison study of UWB indoor channel models," *IEEE Trans. on Wireless Communications*, Vol. 6, No. 1, Jan. 2007.
31. Alvarez, A., G. Valera, M. Lobeira, R. Torres, and J. L. Garcia, "New channel impulse response model for UWB indoor system simulations," *Proc. VTC 2003 Spring*, 1–5, 2003.
32. Pagani, P. and P. Pajusco, "Experimental assessment of the UWB channel variability in a dynamic indoor environment," *Proc. IEEE PIMRC*, Vol. 4, 2973–2977, 2004.
33. Braun W. R. and U. Dersch, "A physical mobile radio channel model," *IEEE Trans. on Vehicular Technology*, Vol. 40, No. 2, 472–482, May 1991.
34. Beckmann, P. and A. Spizzichino, *The Scattering of Electromagnetic Waves from Rough Surfaces*, Macmillan, New York, 1963.
35. Yacoub, M. D., "The α-μ distribution: A physical fading model for the stacy distribution," *IEEE Trans. on Vehicular Technology*, Vol. 56, No. 1, 27–34, Jan. 2007.